Insights into Ultrashort Laser-Driven Au:TiO 2 Nanocomposite Formation

Yaroslava Andreeva, Nipun Sharma, Anton Rudenko, Julia Mikhailova, Maksim Sergeev, Vadim P Veiko, Francis Vocanson, Yaya Lefkir, Nathalie Destouches, Tatiana Itina

THE JOURNAL OF PHYSICAL CHEMISTRY C

pubs.acs.org/JPCC Article

Insights into Ultrashort Laser-Driven Au:TiO_2 Nanocomposite Formation

Yaroslava Andreeva,* Nipun Sharma, Anton Rudenko, Julia Mikhailova, Maksim Sergeev, Vadim P. Veiko, Francis Vocanson, Yaya Lefkir, Nathalie Destouches, and Tatiana E. Itina*

Cite This: J. Phys. Chem. C 2020, 124, 10209–10219

ABSTRACT: Modern methods of laser-based nanocomposite fabrication and treatment rely on a deep understanding of the interplay between a set of mechanisms involved, such as nanoparticle growth and decay, material phase transformation, degradation, and damage. In this work, scanning multipulse femtosecond laser irradiation is used for Au:TiO_2 nanocomposite formation. Depending on laser scan speed, two different regimes are observed revealing different gold nanoparticle growth rates. The regime of the remarkably fast laser-induced growth of Au nanoparticles is found to be accompanied by the cavity formation in titania film around the particles. The transition between two formation regimes is found to be abrupt, confirming the catastrophic mechanism of Au nanoparticle growth. The obtained results are analyzed based on the developed numerical model including effects such as nanoparticle absorption, local field enhancement, photoinduced free carrier generation, plasmon-assisted electron emission, and thermal heat transfer from nanoparticles toward titania matrix. Our modeling reveals the crucial role of collective thermoplasmonic effects caused namely by bimodal nanoparticle size distribution. The performed analysis also suggests that spall in the solid state is responsible for final matrix degradation if nanoparticles become large enough. The considered laser-based formation of optical nanocomposites is crucial not only for the better understanding of ultrashort laser interactions with glass–metallic nanocomposite materials but also for numerous applications in photocatalysts, solar cells, and chemosensors.

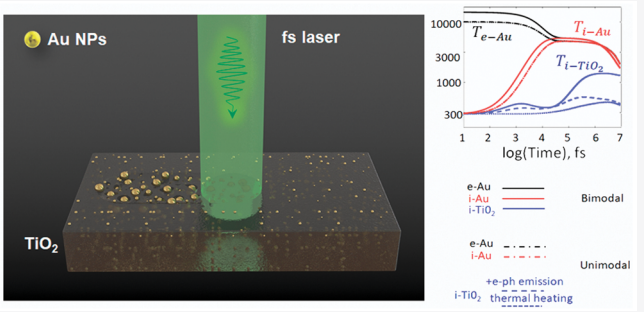

INTRODUCTION

During the past decade, nanocomposite materials based on a transparent matrix with metal nanoparticles (NPs) have become particularly attractive in the growing fields of photonics, catalysis, and security research.[1−3] Many characteristics of such optical nanocomposites are attributed to size distribution and concentration of the embedded metal NPs and are often connected to the local field enhancement around them, as well as to their thermoplasmonic properties. Such effects, such as linear and nonlinear optical properties,[4−6,6,7] as well as chemical reactivity[8] of composite materials were investigated. Among a variety of such composite materials, titanium dioxide-based films attracted tremendous attention due to their high thermodynamic stability within a wide range of temperatures, relatively wide band gap, the difference in the surface layer semiconducting properties from those of the bulk phase, inertness, nontoxicity, as well as low price.[9−11] Moreover, an incorporation of plasmonic NPs considerably enhances light absorption and modifies its range as a result of plasmon resonances.[12,13] As a result, such materials can be effectively used to improve the photocatalytic performance of TiO_2 films due to electron transfer processes in such composites.[14,15] Therefore, semiconducting nanocomposites based on titanium dioxide are promising for the production of the next generation of solar cells, photocatalysts, gas sensors, or UV detectors.[15−19]

Numerous methods were proposed to introduce metal NPs into solid matrices, including chemical and thermal methods, photodeposition, sputtering, and core–shell nanostructure fabrication.[12,20−22] Among them, laser methods are fairly promising as they are able to provide a precise control over material properties[6,23,24] and local modification of the size and distribution of NPs,[23,25] as well as for structural modifications and phase changes of the matrix material.[26,27] In addition, laser methods are safer and cleaner than other methods, since commonly there is no need to use toxic substances.

However, the effect of laser field enhancement, which is advantageous for sensing (SERS), surface lithography, and electronics, can considerably decrease the composite damage threshold becoming the main limiting factor for a number of

Received: February 7, 2020
Revised: April 10, 2020
Published: April 16, 2020

https://dx.doi.org/10.1021/acs.jpcc.0c01092
J. Phys. Chem. C 2020, 124, 10209−10219

optical applications. Indeed, resonant absorption, as well as other effects taking place under femtosecond laser irradiation, such as local field enhancement, photoinduced free carrier generation, plasmon-assisted electron emission, and thermal heat transfer, may lead to a considerable undesirable overheating and favors material damage.[28] The insights of NPs influence on the porosity and structure of different materials were discussed by different research groups. Previously, bubbles, pores, or cavities were found to be formed around laser-irradiated NPs in the presence of either a liquid or a solid surrounding medium. The bubble/pore formation fluence threshold strongly depends on NP size with a minimum around the maximum in Q_{abs}.[29−32] These bubbles or cavities result from one or several of the three main effects: (i) heat transfer from NPs to the ambient medium through heat convection, (ii) heat transfer via heat conduction, and (iii) plasma-mediated medium heating due to the field enhancement and local ionization of the surrounding medium. While the first and the second ones are common for all the lasers,[29,32,33] the third mechanism is mostly observed in the case of a sufficiently powerful femtosecond laser irradiation with resonant plasmonic NPs.[30] For a solid matrix, additional energy is required for matrix melting, softening, and spall. Here, the term "spall" denotes the effect of material spalling or spallation, referring to a process of mechanical material failure caused by the formation of a sufficiently high tensile stress overcoming material mechanical strength.[34] The general trends are, however, similar in the case of liquid and solid matrix. In the bulk, such an effect may lead to the formation of a small cavity that can either grow or shrink with time.[35] The main difference is that metallic NPs are expected to be cooled much faster in the presence of a denser medium. Nevertheless, in a solid matrix, larger particles are also known to stay hot for a longer time compared to the smaller ones.

A better understanding of laser-induced Au NPs growth in solid matrices is also challenging. Despite several studies in this field,[23,36,37] the mechanisms of NPs growth in solid media remain particularly poorly understood in the case of ultrashort femtosecond laser irradiation. Such understanding is, however, crucial to achieve uniform and controllable properties of the optical nanocomposite, which are important for advanced applications.

In this paper, we experimentally and numerically investigate both the formation and degradation of Au:TiO_2 nanocomposite thin film under scanning femtosecond laser irradiation. In particular, two different types of nanostructures are found to be formed depending on the laser scan speed. The nanoparticle distribution was analyzed for different processing regimes. We also analyze the NP's size effect on the absorption of the nanocomposite material. The observed changes in the absorption spectra of TiO_2:Au-based nanocomposites are examined. Particularly the role of the presence of two nanoparticle populations, larger and smaller ones, on thermoplasmonic properties is emphasized. Based on the experimental and numerical results, the mechanism of Au NPs growth in titanium dioxide matrix is proposed. Numerical simulations are then performed to elucidate the mechanisms leading to the material damage and nanocomposite degradation.

EXPERIMENTAL AND THEORETICAL METHODS

Samples Preparation. The experiments were carried out with TiO_2 porous thin films containing gold NPs dip-coated on a glass substrate. The mesoporous films were elaborated by a sol−gel synthesis with titanium tetraisopropoxide (TTIP, Aldrich; 97%).[38] To introduce gold NPs into the porous media, we soaked the film in 10 mmol $HAuCl_4$ aqueous solution and then in 10 mmol $NaBH_4$ aqueous solution 20 times in sequence. Sodium borohydride was used to ensure the initial laser absorption of the samples. After that, the samples were rinsed in pure water and dried at room temperature. The resulting film with a thickness of about 180 nm contained small Au NPs with diameter from 5 to 7 nm and was slightly pink.

Laser Irradiation. A femtosecond laser (Pharos) was used, providing laser pulses at 1030 nm central wavelength with maximum pulse energy of 10 μJ, and pulse duration of 190 fs at the repetition rate of 610 kHz. For the sample irradiation, the second harmonic (λ = 515 nm) provided by a BBO crystal was utilized. The average laser power was varied by using a polarizer−attenuator within a range from 160 to 220 mW. The linearly polarized focused laser Gaussian beam with the estimated diameter of d_0 = 20 μm ($1/e^2$) scanned the surface line-by-line with two-coordinate motorized translations (PL Micos) providing the constant displacement along the Y-axis, dy = 2 μm. To control the growth of Au NPs, the laser fluence and scan speed were varied from 42 to 57 mJ/cm^2 and 0.16 to 1.6 mm/s, respectively.

Characterization. To investigate the film morphology, a scanning electron microscope (SEM), FEI Nova nano SEM 200 model equipped by helix detector was utilized in low-vacuum mode before and after laser treatment. UV−visible transmission spectra were measured with a Cary 5000 spectrophotometer (Agilent). Surface topology of the samples was measured by atomic force microscopy (AFM, NT-MDT Nanoeducator).The average roughness was calculated as a root-mean-square of N height points of the measured field.

Modeling Details. Depending on the NP size and concentration, the absorption, scattering, and propagation of laser irradiation are strongly affected by the plasmonic NPs grown in the nanocomposite material. To examine this effect, a series of simulations are performed first by using the classical Mie theory.[39,40] Absorption efficiency is calculated as a function of the NP's size for the given laser wavelength. Based on the sample-imaging results, this approach describes the case when NP concentration is low enough, so that they are considered independently. The incident laser is simulated as a plane wave (λ = 0.515 μm, linear polarization) interacting with a single gold nanosphere surrounded by a TiO_2 matrix (refractive index n = 1.6). For modeling of field distribution, a finite elements approach for a single particle in the matrix was used (Figure 4d below).

Then, a much more detailed model is developed providing a solution to the equation systems self-consistently describing electromagnetic field, material ionization, and three-temperature thermodynamics for an ensemble of particles with different size distributions that are commonly formed in the matrix under the considered laser-irradiation conditions. Temperature fields and the dynamics of nanocomposite material containing different nanoparticle populations and concentrations are calculated by using the three-temperature model considering the localized surface plasmon excitation, photoinduced free carrier generation, plasmon-assisted electron emission, and thermal heat transfer (see details in the Discussion section).

RESULTS

Laser-Induced Nanoparticle Formation. The initial film contained only small NPs with diameter less than 10 nm. Before

https://dx.doi.org/10.1021/acs.jpcc.0c01092
J. Phys. Chem. C 2020, 124, 10209−10219

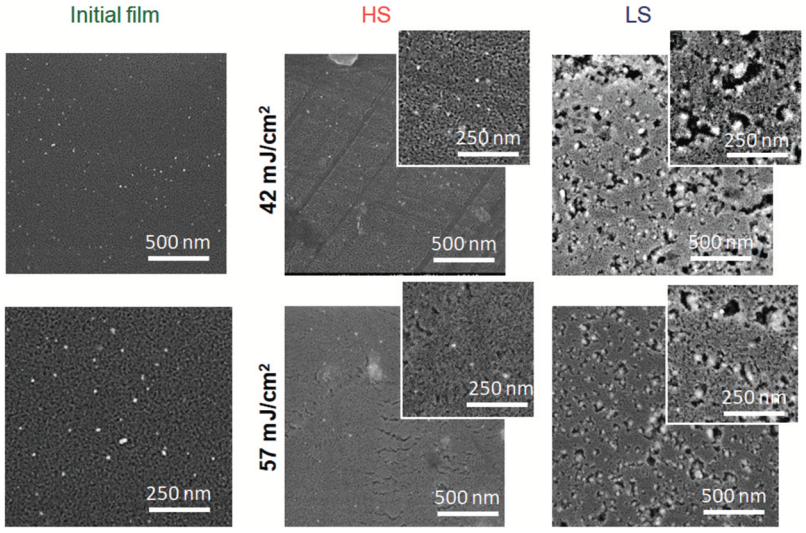

Figure 1. SEM images of the film before and after treatment. Laser fluence $F = 42$ and 57 mJ/cm^2, scan speed for LS structures is 0.16 mm/s, and for HS structures it is 1.6 mm/s.

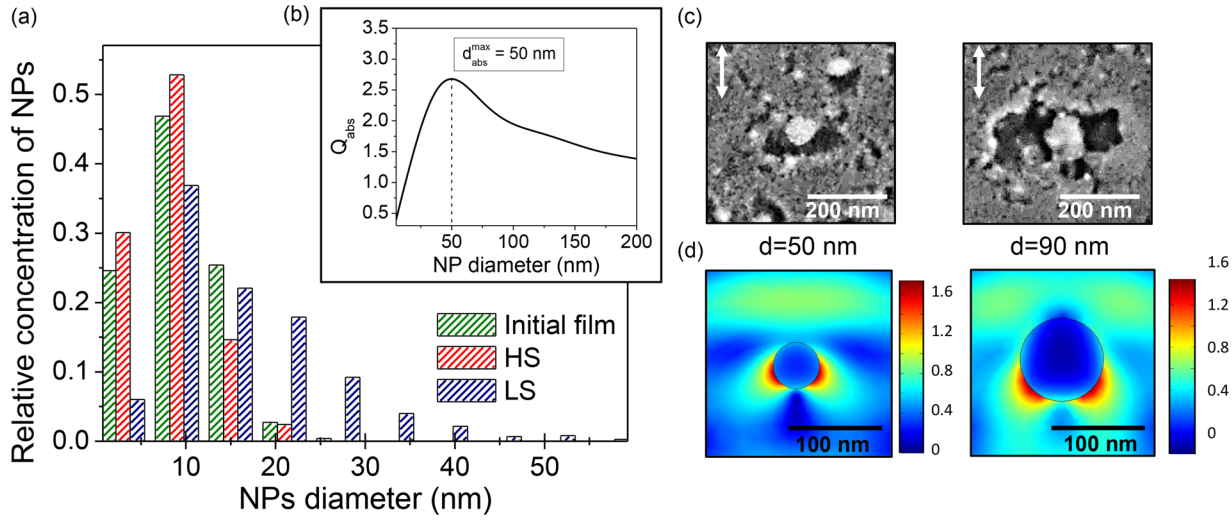

Figure 2. (a) Size distribution of gold NPs in the film before and after laser treatment. Laser fluence $F = 57$ mJ/cm^2, scan speed for the LS structures is 0.16 mm/s, and for the HS structures it is 1.6 mm/s. (b) Calculated absorption efficiency of the nanocomposite based on TiO_2 as a function of the diameter of gold NPs (refractive index of the surrounding media $n = 1.6$, for $\lambda = 515$ nm). (c) SEM images of the NPs produced in LS mode ($F = 57$ mJ/cm^2, $V_{sc} = 0.16$ mm/s) (top view picture). Double arrow represents polarization of incident laser irradiation. (d) Calculated field distribution of gold nanoparticles in TiO_2 ($n = 1.6$, for $\lambda = 515$ nm) for spheres with the diameters of 50 and 90 nm (side view picture).

the laser treatment the film was rather smooth without any visible cracks or impurities. The average pore size was 5−7 nm.

The samples were subjected to a scanning laser irradiation line-by-line covering a 2.5 × 2.5 mm area. The displacement between two lines was 2 μm, providing an overlap of laser tracks of 500 lines/mm. Figure 1 demonstrates the SEM images of the surface before and after laser treatment.

Depending on the scan speed, two different regimes were observed: (i) At a high scan speed $V_{sc} = 1.6$ mm/s (HS), the obtained structures are very close to the initial film. In this case, the porosity remains the same, but the concentration of the gold NPs on the top is the same or even lower than in the initial film. (ii) At a low scan speed $V_{sc} = 0.16$ mm/s (LS), the NPs' growth occurred. The large cavities were observed at the surface. Note that the observed results also depend on laser fluence, but only below a certain threshold. In the case of HS structures, a set of small cavities was also observed in the film, but only for laser fluence larger than $F = 52$ mJ/cm^2.

To better understand the difference between the LS and the HS structures, an analysis of the NP relative concentration on the surface was performed. The size distributions of gold NPs are shown in Figure 2 for different laser scan speeds. Before laser treatment NPs had a mean size of 9.7 nm (standard deviation of ∼4.4 nm). After the HS processing, mean size slightly decreased to 8.7 nm (standard deviation of ∼3.5 nm), and the relative concentration of the NPs larger than 15 nm decreased almost by a factor of 2 on the surface compared to the initial film. On the contrary, after the LS processing the NPs mean size doubled and reached the value of 16 nm (standard deviation of ∼9.3 nm). NPs' concentration significantly increased (Figure 2), and their size increased so that one could observe bigger NPs with the average diameter larger than 20 nm.

https://dx.doi.org/10.1021/acs.jpcc.0c01092
J. Phys. Chem. C 2020, 124, 10209−10219

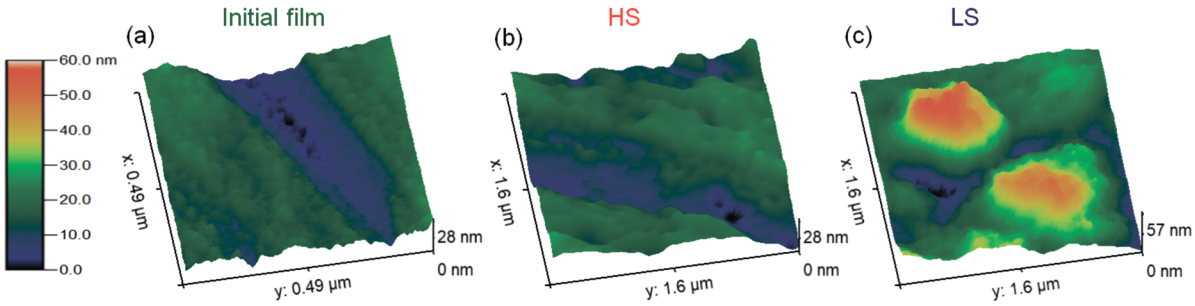

Figure 3. 3D surface topology of the samples before and after laser treatment obtained by AFM. Laser fluence F = 57 mJ/cm^2, scan speed for LS structures is 0.16 mm/s, and for HS structures it is 1.6 mm/s.

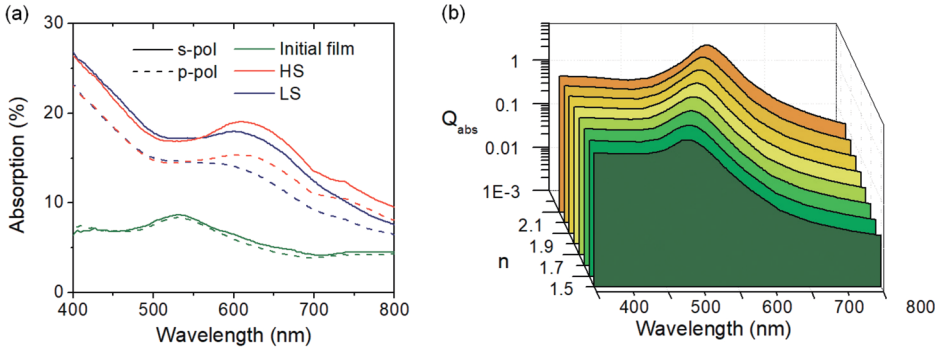

Figure 4. (a) Absorption spectra of the samples before and after laser treatment. Laser fluence F = 57 mJ/cm^2, scan speed is 0.16 mm/s for LS structures, and it is 1.6 mm/s for HS structures. Solid and dashed lines correspond to s-polarization and p-polarization of probe light, respectively. (b) Simulated absorption efficiency of the nanocomposite for different refractive indices of surrounding media. Colors correspond to spectral maximum wavelengths.

To understand how the NP size influences the absorption of laser irradiation, the absorption efficiency was calculated as follows:[29]

$$Q_{\mathrm{abs}}^{\lambda} = \frac{4\cdot\sigma_{\mathrm{abs}}^{\lambda}}{\pi d^2} \tag{1}$$

where σ_{abs} is the absorption cross section and d is the NP diameter. Both the absorption efficiency and the absorption cross section of the NP depend on the laser wavelength. The absorption cross section is calculated by using the complete Mie theory.[40]

For NPs with a diameter larger than 20 nm, the absorption efficiency Q_{abs} is much higher than for smaller ones (Figure 2b). This result is attributed to the plasmonic properties of gold NPs. In fact, the localized surface plasmon resonance (LSPR) is known to depend on the nanoparticle size. The maximum absorption is thus expected for the particle diameter of 50 nm corresponding to the SPR maximum at the considered laser wavelength. For such NPs, the near-field enhancement of more than 1.5 times is obtained (Figure 2c). The slightly enhanced field observed above the particle is the result of laser light scattering on the particle and is visible in a side view. When the nanoparticle size increases above the dipole approximation, additional modes enter into play (e.g., quadrupole modes), and the particle scatters more than it absorbs. This effect is correctly reproduced by the complete Mie theory. Therefore, for larger NPs both the calculated absorption efficiency and the field enhancement are smaller.

Furthermore, large NPs also affect the porosity and structure of the TiO_2 film: Figure 2d clearly demonstrates the cavity development in the vicinity of the NPs. To better understand the value of the formed cavities, surface topology was then investigated. It is found that the surface relief was also varied depending on the scan speed. Figure 3 shows the three-dimensional surface topologies of the film obtained by AFM before and after the ultrashort laser processing. The corresponding surface profiles are shown in Figure S1 of the Supporting Information. For the initial film (Figure 3a), the height deviation did not exceed 10 nm, and the average roughness was 5 ± 1 nm. The maximum height of relief reached about 15 nm, and the average roughness was 5 ± 1 nm for the HS structures (Figure 3b). As a result of laser exposure at LS, the average roughness increased up to 6 ± 1 nm; however, the film relief changed dramatically (Figure 3c). The rails corresponding to cavities in the film reached 35−40 nm. Therefore, the average roughness before and after treatment did not significantly change, whereas the surface relief became more developed for LS.

Optical Properties. Under laser irradiation, both the matrix porosity and crystal structure are modified. This result agrees with previous observations of Sharma et.al.,[27] where laser heating of sol−gel titania films resulted in crystal growth and in the phase modification, also affecting the refractive index of such films. As a result, not only the structure but also the optical properties of the material can be controlled.

Figure 4a demonstrates the absorption spectra measured for the considered nanocomposite films. Before laser treatment, the film exhibited an absorption peak corresponding to the plasmon resonance of Au NPs in TiO_2. Interestingly, after the laser irradiation at HS and LS, the peak red-shifted to 606 and 600 nm, respectively.

The peak shifts are due to several factors, such as a change in the NP concentration, size distribution and mean size, as well as a modification of the matrix optical properties. The presented

https://dx.doi.org/10.1021/acs.jpcc.0c01092
J. Phys. Chem. C 2020, 124, 10209−10219

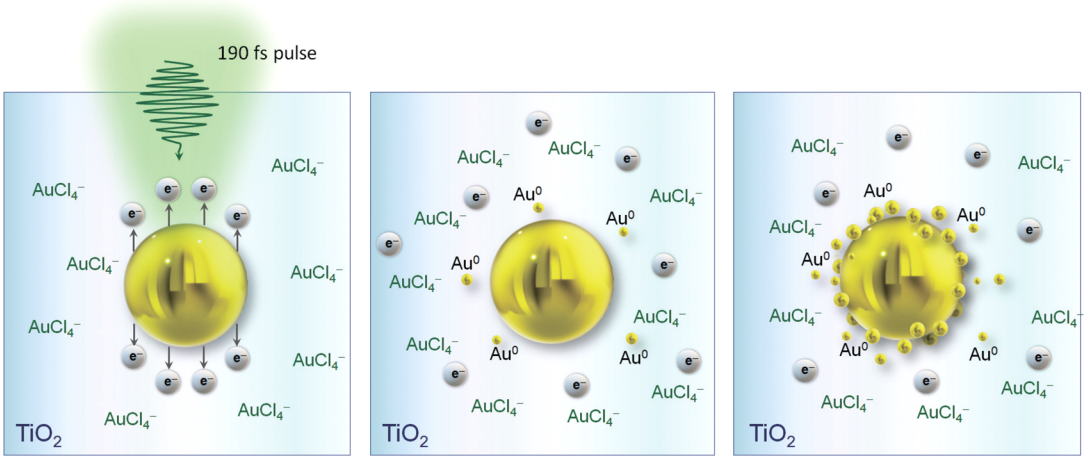

Figure 5. Sketch of Au NPs growth mechanism under femtosecond laser exposure.

SEM images show that the size of NPs dramatically varies on the surface only for the LS structures, whereas the peak position is close for the laser-treated and initial samples. To analyze the effect of sol−gel refractive index modification on the film absorption spectrum, we calculated the absorption efficiency of the nanocomposite material with Au NPs for different refractive indices of the surrounding media. The size distribution of gold NPs corresponded to the one typically obtained in the HS structures (Figure 3a). For the initial film, the peak agrees with that of the absorption efficiency for the material with matrix refraction index $n = 1.4$. In this case, the presence of small NPs slightly influences the peak position because the absorption efficiency of NPs smaller than 10 nm (Figure 2b) is negligible. On the other hand, laser processing leads to the considerable temperature rise triggering a set of phase transitions and a pronounced change in the reflective index. The peak positions of the measured absorption spectra are close to the calculation results for n from 1.9 to 2.1. This result confirms the fact that the material experienced strong structural modification upon laser irradiation. The difference between the absorption spectra for s- and p- polarization usually appears due to several effects. Among them we can mention sample anisotropy, the formation of periodic structures along one of the polarization directions, an elongation of the nanoparticles shape along one of the axes, etc. Here, a slight dichroism of experimental spectra apparently results from the modifications of structure and crystal phase of TiO_2 matrix.

DISCUSSION

Thus, two significant effects were observed in the nanocomposite films under femtosecond laser irradiation: the rapid growth of Au NPs and the TiO_2 film modifications going up to the film damage. Next, we consider the physical background aspects of the mechanisms involved in these effects.

Laser-Induced Gold Nanoparticle Growth. Gold nanoparticles grow under the presented irradiation conditions, as illustrated in Figure 5. First, laser heats free electrons in gold nanoparticles. According to the nanoparticle plasmonic properties, part of the field-driven electrons can be emitted from the resonant Au NP's surface during the femtosecond laser pulse. The injected electrons then participate in the reduction of the $AuCl_4^-$ ions. As a result, Au NPs grow more efficiently.

We note that the fraction of the metallic phase in the LS structures is significantly higher than that in the initial film. Thus, $HAuCl_4$ acts as a donor of Au atoms. The reduction of the chlorine complex to metallic form can be described by the following reaction:[41]

$$[AuCl_4]^- + 3e^- = Au^0 + 4Cl^-,\ E_0 = 0.994\ V \qquad (2)$$

To drive the Au ion reduction, three electrons are required. As a result, the reduction threshold is rather sharp. To initiate this process, the multiple-pulse ultrashort laser irradiation is found to be very efficient. On the other hand, electrons are also trapped in the matrix surrounding the NPs providing an increase in the absorption for the following laser pulses.

After the laser pulse, the gold nanoparticle cools down by heat exchange with the matrix and by heat conduction giving rise to hot spot formation and thermoplasmonic effects. The gold atoms that appeared start to condense and merge leading to additional smaller "daughter" NP growth around the "mother" NPs. The material around the NP is heated, causing not only matrix phase changes and structural modifications but also local damage in the vicinity of the hot spots at higher absorbed laser energies. All these processes contribute to the laser-induced step-by-step final nanocomposite formation.

Film Degradation Mechanism. Femtosecond laser-induced heating of transparent matrix containing plasmonic NPs is realized via multiple physical mechanisms occurring on different time scales. During laser pulse propagation, the electric field was strongly enhanced close to the surface of NPs due to the localized surface plasmon excitation.[42,43] Even stronger near-field enhancement was achieved if the NPs were located close enough to each other. As a result, the optical breakdown of dielectric occurs, and free carriers were generated by photo-ionization and avalanche ionization processes,[44] changing the transient optical properties. This transient modification leads to the additional absorption and lattice heating during electron−ion transfer on picosecond time scales.

Free electrons were also generated via electron photoemission from plasmonic NPs toward transparent matrix.[45−48] Two effects are relevant here: (i) a spherically symmetric bulk mechanism, when an electron absorbs a photon in the metal; and (b) a polarization-dependent surface mechanism, when an electron absorbs a photon in a collision with the metal surface.[46] The volume effect dominates for ultraviolet wavelengths and strongly depends on the NP size.[45,48] The surface effect becomes more pronounced for near-infrared wavelengths.[46] Again, higher

https://dx.doi.org/10.1021/acs.jpcc.0c01092
J. Phys. Chem. C 2020, 124, 10209−10219

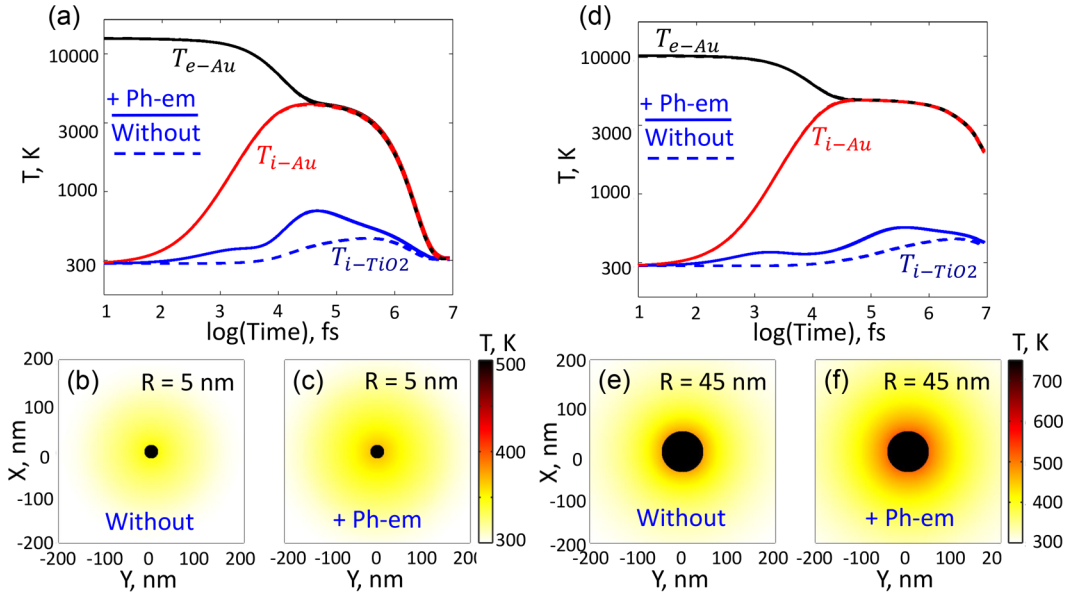

Figure 6. Electron (black solid) and ion temperature (red solid) of gold and titanium dioxide temperature (blue solid) dynamics in the vicinity of contact with NP (a) of $R = 5$ nm and (d) of $R = 45$ nm upon $F = 50$ mJ/cm^2 irradiation. Blue dashed line indicates temperatures attained if heating from a single NP without electron photoemission is considered. (b–c, e–f) Snapshots of matrix temperature distribution at 1 ns after thermal transfer between NPs and titania (b, e) without taking into account electron photoemission or (c, f) including this effect. Gold NPs of (b–c) $R = 5$ nm and (e–f) $R = 45$ nm are centered at (0, 0).

NP concentration affects the efficiency of electron photoemission.

Finally, the matrix was heated via classical thermal transfer from hot NPs toward cold lattice on longer time scales (100 ps–1 ns).[49−52] The amount of transferred energy is inversely proportional to the NPs' size. However, the heat is further diffused in a matrix via thermal conduction. Transparent matrix heated by smaller NPs cools down much faster than it is heated by larger NPs.[49] Therefore, the temperature dynamics are complicated by different populations and concentrations of the grown NPs. The characteristic cooling time and the efficiency of photoinduced heating affect possible phase transitions, i.e., melting of the transparent matrix, but also the mechanical properties of the nanocomposite resulting in an undesirable damage if the critical stress is overcome. A complex interplay of nontrivial physical processes, concurrently influencing temperature distributions inside nanocomposite, requires accurate multiphysical modeling at the nanoscale. Here, we unify several approaches in order to evaluate the importance of each described effect.

Herein, field distribution inside and outside the NPs and electron plasma kinetics in titanium dioxide are first modeled by solving nonlinear Maxwell equations coupled to a single rate equation. The corresponding numerical method is described in ref 53.

First, the quantum efficiency of photoelectron emission η is accessed by computing the integral for surface and volume photoelectron emission from ref 45 for $\lambda = 515$ nm wavelength excitation, $E \approx 2.4$ eV (mean-free path $l_e = 30$ nm for gold[54]), and specific NP radius R, yielding $\eta \approx 2 \times 10^{-2}$ for $R = 45$ nm and $\eta \approx 5 \times 10^{-2}$ for $R = 5$ nm. The electron spill-out distribution around the nanoparticle is obtained from the rate of quantum efficiency, total charge conservation, and exponential decay of the electron density in the matrix from the nanoparticle interface $N_e(r) = N_0 \cdot [1 + \exp(\alpha(r - R))]^{-1}$,[55,56] where $N_0 = 5.9 \times 10^{28}$ m^{-3} is the equilibrium electron density of gold.

Then, total free carrier density N_e generated by ionization processes is obtained by solving the single rate equation written as

$$\frac{\partial N_e}{\partial t} = W_{PI}(I) + N_e W_{AI}(I) \tag{3}$$

where W_{PI} is the photoionization rate given by the Keldysh formula for $E_g = 3$ eV electron bandgap, $\lambda = 515$ nm, and $n = 1.6$ refractive index. W_{AI} is the avalanche ionization rate estimated by the Drude equation. Based on the solution of the coupled equations, the time evolution of electron density N_e, nonlinear current $\vec{J}$, and electric field $\vec{E}$ are accessed and further used to calculate the temperature distribution.

The three-temperature model[50−52] is applied to capture thermal transfer between gold nanoparticles and titanium dioxide matrix

$$\begin{cases} C_e \dfrac{\partial T_e}{\partial t} = \nabla \cdot (k_e \nabla T_e) - \gamma_{ei}(T_e - T_i) + \vec{J}\vec{E} \\ \rho_{NP} C_{NP} \dfrac{\partial T_{NP}}{\partial t} = \nabla \cdot (k_{NP} \nabla T_{NP}) \\ + \gamma_{ei}(T_e - T_{NP}) + 3h(T_m - T_{NP})/R_{NP} \\ \rho_m C_m \dfrac{\partial T_m}{\partial t} = \nabla \cdot (k_m \nabla T_m) \\ + \gamma_{ei}(T_e - T_m) + 3h(T_{NP} - T_m)/R_{NP} \end{cases} \tag{4}$$

where T_e, T_{NP}, and T_m are electron, NP, and transparent matrix temperatures, respectively. The $\vec{J}\vec{E}$ is calculated by solving nonlinear Maxwell equations and corresponds to the energy transferred to Joule heating. For gold, the electronic properties C_e, k_e, and γ_{ei} are evaluated as a function of electron temperature following ref 57 for heat capacity and electron–ion coupling factor and ref 58 for thermal conductivity. For titanium dioxide,

https://dx.doi.org/10.1021/acs.jpcc.0c01092
J. Phys. Chem. C 2020, 124, 10209−10219

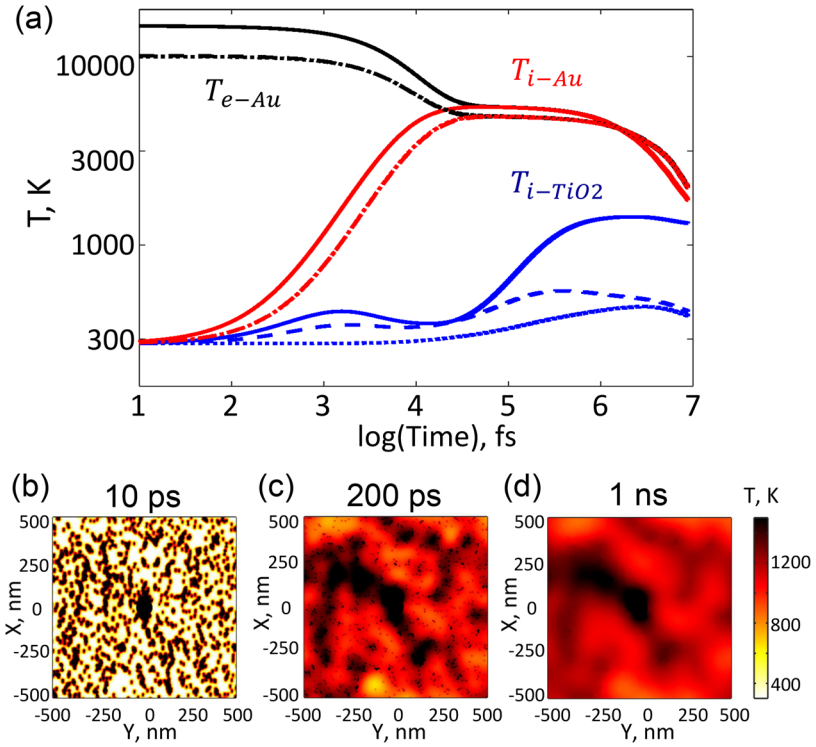

Figure 7. (a) Electron (black solid) and ion temperatures (red solid) for the gold NP with R = 45 nm and titanium dioxide temperature (blue solid) dynamics in the vicinity of the contact calculated with F = 50 mJ/cm^2. The collective heating induced by smaller NPs with R = 5 nm, electron photoemission from NPs, and free carrier generation by ionization processes in titanium dioxide are included. The blue dotted line indicates the temperatures attained if heating only from a single NP is considered, whereas the blue dashed line additionally includes the electron photoemission effect. For a single NP, the electron and ion temperatures of gold are indicated by black and red dash-dotted lines, respectively. (b–d) Snapshots of the matrix temperature distribution at (b) 10 ps after electron–ion transfer, (c) 200 ps after irradiation, and (d) 1 ns after thermal transfer between NPs and titania. Gold NP of R = 45 nm is centered at (0, 0), whereas smaller NPs of R = 5 nm are distributed randomly with concentration of 500 particles per 1 μm^2.

the expressions for an ideal Fermi gas are applied, where $C_e = 3/2k_BN_e$, $\gamma_{ei} = C_e/\tau_{ei}$ with τ_{ei} = 1 ps, and thermal conductivity k_e is assumed to be negligible during electron–ion transfer. The thermal transfer between gold NPs and titanium dioxide is described by $3h(T_m - T_{NP})/R_{NP}$, where $h \approx 100$ MW/m^2/K is the energy exchange coefficient[49−51] and R_{NP} is the NP radius. For gold, ρ_{NP} = 19.3 g/cm^3, whereas C_{NP} and k_{NP} are evaluated as a function of ion temperature as in ref 59. For titanium dioxide, ρ_m = 4.23 g/cm^3, C_m = 712 J/kg/K, and k_m = 10.3 W/m/K are set.

The performed three-dimensional multiphysical simulations yielded not only the distribution of the electromagnetic field and free carrier density but also temperature fields for single NPs and for the case of different NP populations. These several gold nanoparticle populations result from multiple-pulse irradiation, where several femtosecond laser pulses have participated in the nanoparticle growth.

The results of the calculations performed for a single gold particle of R = 5 and 45 nm are presented in Figure 6. The NPs are heated up to the electron temperature $T_e \approx$ 10 000 K and then relaxed to the ion temperature $T_i \approx$ 3 500 K during ≈20 ps, slightly dependent on the NP size.

In fact, the electron–phonon coupling in metal nanoparticles or clusters was found to deviate from the bulk metal response as the characteristic sizes decrease down to a few nanometers.[60,61] Such a deviation can contribute to the changes in the imaginary part of dielectric permittivity[62] and to the faster energy transfer between electrons and lattice.[60] For gold nanoparticles, however, such an effect is significant only for R < 5 nm (correction of ≈5% for R = 5 nm);[60,61] therefore, it is safely neglected in simulations. The observed difference in simulations between electron–ion transfer times in the case of R = 5 and 45 nm is related mostly to different maximum electron temperatures, slightly higher in case of a smaller nanoparticle. In fact, the absorbed energy distributions for R = 5 nm nanoparticle below the absorption length and for R = 45 nm above the absorption length for gold are qualitatively different themselves, triggering nonequivalent field enhancements on the nanoparticle interface for the same applied laser fluence.

The applied fluence F = 50 mJ/cm^2 is one order smaller than the one required for an optical breakdown in the narrow band gap dielectrics or semiconductors[63] at λ = 515 nm. Photoionization is reinforced by the electric field enhancement ≈2–3 at the NPs surface. However, this process produces the number density of free carriers on the order of 10^{24}–10^{25} m^{-3}, which is still not enough to considerably affect matrix heating. The blue dashed lines in Figure 6a, d show the temperature dynamics in the absence of electron photoemission, i.e., the heating effect only due to the heat transfer from the plasmonic NP and to the NP cooling in the presence of the titania matrix. The maximum matrix temperature is achieved after ≈300 ps for R = 5 nm and after ≈2 ns for R = 45 nm.

Matrix material is found to be hotter around the nanoparticles with R = 45 nm than with R = 5 nm after 1 ns. This result can be explained by the fact that the nanoparticle cooling is much longer for R = 45 nm than for R = 5 nm. If the electron

https://dx.doi.org/10.1021/acs.jpcc.0c01092
J. Phys. Chem. C 2020, 124, 10209–10219

photoemission is included, the free carrier number density of the order of 10^{27} m^{-3} is no longer negligible; therefore, titania is preheated by the electron plasma at several picoseconds after the electron−ion transfer. This preheating plays an important role in defining the matrix maximum temperature, which reaches ≈650 K near nanoparticles with R = 5 nm and ≈500 K for R = 45 nm. Interestingly, cooling dynamics are very similar to the previous case, where titania with smaller NP cools down abruptly, whereas titania with larger NP resists a longer time. For instance, much higher temperatures are established after 1 ns as shown in Figure 6c, f, although the maximum temperature is 150 K less.

Thus, although the electron photoemission plays a significant role on the picosecond time scale, the heat transfer from the gold NP is the main effect. Moreover, thermoplasmonc effects and, particularly, nanoparticles cooling dynamics are crucial for better control of the laser-induced nanocomposite modifications.

To better understand the obtained experimental findings, collective nanparticle heating effects were then included in the model. For this, we considered a nanoparticle with R = 45 nm surrounded by many smaller NPs of R = 5 nm. Based on the typical experimental values, the concentration of small NPs was set to be 500 particles per 1 μm^2. The calculation results are shown in Figure 7, where two pronounced local maxima are evidenced in temperature dynamics: (i) heating due to free carriers generated mostly by electron photoemission and partly by photoionization processes at 10 ps and (ii) heating due the collective thermal transfer from gold NPs at ≈400 ps, finally reaching ≈1500 K in the vicinity of the bigger NP. The temperature distributions are shown in Figure 7b−d. After electron−ion transfer, the temperature distribution is still strongly inhomogeneous, where the black points correspond to the positions of randomly distributed gold NPs and the titania matrix is only slighly preheated in the vicinity of these hot spots in Figure 7b. Then, the heat from smaller NPs is diffused in the whole matrix with more pronounced temperature valleys in the vicinity of the large NP but also where the small NPs are close enough to each other in Figure 7c. This snapshot is taken within 200 ps, before the gold NPs start to cool down abruptly; therefore, their positions are still visible as small hot spots. After 1 ns, the highest temperatures of order ≈1500 K are conserved in the vicinity of the larger NP, whereas the matrix temperature distribution around smaller NPs becomes more homogeneous. Further temperature dynamics are described by homogeneous heating of the lattice, preserving the local maxima established at 1 ns.

The experimental observations and simulations suggest that there were no signs of matrix melting upon laser processing with F = 42−57 mJ/cm^2 and the highest number of pulses. The damage in the vicinity of large NPs evidenced in Figure 2d can be then the result of spall in the solid state, causing cracking or breaking of the titanium dioxide matrix.[34] Grady's balance criterion is commonly applied to define the dynamic conditions of the material degradation due to the applied elastic stress.[35,64,65] To produce any fracture, kinetic and elastic energy should be higher than the surface energy

$$\frac{P^2}{2\rho_m {c_0}^2} + \frac{\rho_m \epsilon^2 s^2}{120} \geq \frac{3K^2}{\rho_m {c_0}^2 s} \quad (5)$$

where c_0 = 6.9 km/s is the speed of sound in titanium dioxide, $P = \rho c_0^2 \epsilon t$ is the dynamic tensile strength, $K = 3.2 \times 10^6$ Pa·m$^{1/2}$ is the fracture toughness, $\epsilon = -\frac{\Delta\rho}{\rho_m \Delta t}$ is the strain rate, $\Delta\rho = \beta T_m$ is the density change, corresponding to material expansion with $\beta = 9 \times 10^{-6}$ K^{-1}, and Δt is the characteristic time of the deformation and the fragment size $s < 2c_0 t$. The minimum time for spall in a solid is defined as $t > \left(\frac{\sqrt{3}K}{\rho c_0 \epsilon}\right)^{2/3} / c_0$.

The temperature dynamics of titania are accessed by the numerical simulations for R = 5 and 45 nm (see Figure 6a, b). Then, the strain rates are determined according to the exposed time and the thermal expansion of the matrix. The calculated elastic and kinetic energies are finally compared to the surface energy according to Grady's criterion. For instance, if the matrix remains as hot as T_m = 1500 K during t = 1 ns time before it cools down, as in the case of a bigger central nanoparticle in Figure 7d, the strain rate reaches $\epsilon = 1.5 \times 10^{-7}$ s^{-1} and the fracture time occurs to be within ≈800 ps. As a result, the damage around the central nanoparticle in Figure 7 is likely to occur. In contrast, for smaller NPs, heat is quickly dissipated (300 ps scale) to lower temperatures below T = 1000 K (compare the maximum temperatures in the matrix far from the central nanoparticle in Figure 7c and in Figure 7d), and the strain rates within cooling time are weaker and not enough to overcome the surface energy. Therefore, Grady's criterion and numerical simulations explain why the damage occurs only in the vicinity of larger NPs for fluences exceeding $F \approx 50$ mJ/cm^2 after irradiation by a higher number of pulses or with lower scanning speed, whereas the titanium dioxide remains entirely in the solid state.

CONCLUSIONS

To summarize, Au:TiO_2 nanocomposites with different optical properties were formed by multiple femtosecond irradiation. By varying laser fluence and scanning speed, we were able to obtain two different types of nanostructures with different nanoparticle populations and sizes in a wide range from 5 to 50 nm and various surface topologies. The HS laser irradiation regime provides the formation of only small NPs with diameters less than 15 nm. On the contrary, the LS processing guarantees extremely rapid growth of Au NPs. The transition between these two regimes is shown to be abrupt. The effect of NP sizes on the absorption has been related to the plasmonic properties: numerical calculations for gold NPs surrounded by titania film confirmed the absorption enhancement for NPs with diameter ranging from 20 to 100 nm (maximum at around 50 nm). Such resonant absorption is shown to enhance electron injection from metallic NPs to the surrounding semiconductor matrix and contribute to NPs growth. The obtained nanocomposite material exhibited a twofold increase of absorption as compared with an initial surface, and for both HS and LS the resonance peak red-shifted from 528 to 600−610 nm.

The mechanisms involved in NPs growth and the following TiO_2 film degradation are then elucidated. Electrons are emitted from the NPs subjected to femtosecond laser and enabling the reduction of $AuCl_4^-$ ions. The resulting Au atoms then condense into smaller nanoclusters and contribute to the growth of the larger NPs. As a result, two populations of nanoparticles are formed. This effect is crucial for the following nanocomposite heating and hot spot formation. As for the photoionization and electron photoemission, these processes are also involved in the film heating. However, their role in temperature increase and film breakdown is not decisive either for relatively big NPs ($R \approx$ 45 nm) or for smaller ones.

Further investigation revealed the importance of collective thermoplasmonic effects in the nanocomposite film heating and,

https://dx.doi.org/10.1021/acs.jpcc.0c01092
J. Phys. Chem. C 2020, 124, 10209−10219

particularly, in matrix degradation. Importantly, the presence of randomly distributed small NPs in the vicinity of the larger ones allows the matrix temperature to increase up to ≈1500 K. By summarizing the experimental observations and the calculation results, matrix degradation is attributed to the spall leading to the cavity or small pore formation around larger NPs in the regime with higer absorbed laser energy.

The considered Au:TiO_2-based nanocomposites are promising in the fields of new energy sources, sensing, and photocatalysis. A better understanding of the ultrashort laser interactions with such nanocomposite materials, thus, can pave the way for the development of a set of novel applications.

■ ASSOCIATED CONTENT

Supporting Information

The Supporting Information is available free of charge at https://pubs.acs.org/doi/10.1021/acs.jpcc.0c01092.

Surface profiles for the LS and HS structures compared with the initial surface (Figure S1); description of three-dimensional multiphysical simulations (PDF)

■ AUTHOR INFORMATION

Corresponding Authors

Tatiana E. Itina − *ITMO University, Saint Petersburg 197101, Russia; Université Lyon, Laboratoire Hubert Curien, Saint-Etienne 42000, France;* orcid.org/0000-0001-7117-8699; Email: tatiana.itina@univ-st-etienne.fr

Yaroslava Andreeva − *ITMO University, Saint Petersburg 197101, Russia;* orcid.org/0000-0002-0582-3159; Email: andreeva.ym@gmail.com

Authors

Nipun Sharma − *Université Lyon, Laboratoire Hubert Curien, Saint-Etienne 42000, France*

Anton Rudenko − *Arizona Center for Mathematical Sciences and College of Optical Sciences, University of Arizona, Tucson, Arizona 85721, United States;* orcid.org/0000-0002-8915-8319

Julia Mikhailova − *ITMO University, Saint Petersburg 197101, Russia*

Maksim Sergeev − *ITMO University, Saint Petersburg 197101, Russia*

Vadim P. Veiko − *ITMO University, Saint Petersburg 197101, Russia*

Francis Vocanson − *Université Lyon, Laboratoire Hubert Curien, Saint-Etienne 42000, France*

Yaya Lefkir − *Université Lyon, Laboratoire Hubert Curien, Saint-Etienne 42000, France*

Nathalie Destouches − *Université Lyon, Laboratoire Hubert Curien, Saint-Etienne 42000, France;* orcid.org/0000-0002-3843-6382

Complete contact information is available at: https://pubs.acs.org/10.1021/acs.jpcc.0c01092

Notes

The authors declare no competing financial interest.

■ ACKNOWLEDGMENTS

The reported study was funded by RFBR, project number 19-32-90247. A.R. acknowledges the Air Force Office for Scientific Research for financial support under award no. FA 9550-19-1-0032. Y.A. acknowledges support from the scholarship of the President of the Russian Federation.

■ REFERENCES

(1) Pastoriza-Santos, I.; Kinnear, C.; Pérez-Juste, J.; Mulvaney, P.; Liz-Marzán, L. M. Plasmonic polymer nanocomposites. *Nat. Rev. Mater.* **2018**, *3*, 375−391.

(2) Choi, Y.; Cha, S. K.; Ha, H.; Lee, S.; Seo, H. K.; Lee, J. Y.; Kim, H. Y.; Kim, S. O.; Jung, W. Unravelling inherent electrocatalysis of mixed-conducting oxide activated by metal nanoparticle for fuel cell electrodes. *Nat. Nanotechnol.* **2019**, *14*, 245.

(3) Hsu, S.-W.; Rodarte, A. L.; Som, M.; Arya, G.; Tao, A. R. Colloidal plasmonic nanocomposites: from fabrication to optical function. *Chem. Rev.* **2018**, *118*, 3100−3120.

(4) Zhang, D.; Gökce, B.; Barcikowski, S. Laser synthesis and processing of colloids: fundamentals and applications. *Chem. Rev.* **2017**, *117*, 3990−4103.

(5) Kelly, K. L.; Coronado, E.; Zhao, L. L.; Schatz, G. C. The optical properties of metal nanoparticles: the influence of size, shape, and dielectric environment. *J. Phys. Chem. B* **2003**, *107*, 668−677.

(6) Ma, H.; Bakhti, S.; Rudenko, A.; Vocanson, F.; Slaughter, D. S.; Destouches, N.; Itina, T. E. Laser-Generated Ag Nanoparticles in Mesoporous *TiO*$_2$ Films: Formation Processes and Modeling-Based Size Prediction. *J. Phys. Chem. C* **2019**, *123*, 25898−25907.

(7) Bityurin, N.; Alexandrov, A.; Afanasiev, A.; Agareva, N.; Pikulin, A.; Sapogova, N.; Soustov, L.; Salomatina, E.; Gorshkova, E.; Tsverova, N.; et al. Photoinduced nanocomposites—creation, modification, linear and nonlinear optical properties. *Appl. Phys. A: Mater. Sci. Process.* **2013**, *112*, 135−138.

(8) Romanyuk, A.; Oelhafen, P. Evidence of different oxygen states during thermal coloration of tungsten oxide. *Sol. Energy Mater. Sol. Cells* **2006**, *90*, 1945−1950.

(9) Nowotny, J. *Oxide semiconductors for solar energy conversion: Titanium dioxide*; CRC Press: Boca Raton, FL, 2016.

(10) Fei, P.; Shi, Y.; Zhou, M.; Cai, J.; Tang, S.; Xiong, H. Effects of nano-*TiO*$_2$ on the properties and structures of starch/poly (*ε*-caprolactone) composites. *J. Appl. Polym. Sci.* **2013**, *130*, 4129−4136.

(11) Zolfi, M.; Khodaiyan, F.; Mousavi, M.; Hashemi, M. Development and characterization of the kefiran-whey protein isolate-*TiO*$_2$ nanocomposite films. *Int. J. Biol. Macromol.* **2014**, *65*, 340−345.

(12) Honda, M.; Kumamoto, Y.; Taguchi, A.; Saito, Y.; Kawata, S. Plasmon-enhanced UV photocatalysis. *Appl. Phys. Lett.* **2014**, *104*, 061108.

(13) Sugiyama, M.; Inasawa, S.; Koda, S.; Hirose, T.; Yonekawa, T.; Omatsu, T.; Takami, A. Optical recording media using laser-induced size reduction of Au nanoparticles. *Appl. Phys. Lett.* **2001**, *79*, 1528−1530.

(14) Asapu, R.; Claes, N.; Ciocarlan, R.-G.; Minjauw, M. M.; Detavernier, C.; Cool, P.; Bals, S.; Verbruggen, S. W. Electron Transfer and Near-Field Mechanisms in Plasmonic Gold-Nanoparticle-Modified *TiO*$_2$ Photocatalytic Systems. *ACS Applied Nano Materials* **2019**, *2*, 4067−4074.

(15) Yuzawa, H.; Yoshida, T.; Yoshida, H. Gold nanoparticles on titanium oxide effective for photocatalytic hydrogen formation under visible light. *Appl. Catal., B* **2012**, *115*, 294−302.

(16) Roy, S. C.; Varghese, O. K.; Paulose, M.; Grimes, C. A. Toward solar fuels: photocatalytic conversion of carbon dioxide to hydrocarbons. *ACS Nano* **2010**, *4*, 1259−1278.

(17) Fehse, M.; Ventosa, E. Is *TiO*$_2$ (B) the Future of Titanium-Based Battery Materials? *ChemPlusChem* **2015**, *80*, 785−795.

(18) Wang, H.; Qin, P.; Yi, G.; Zu, X.; Zhang, L.; Hong, W.; Chen, X. A high-sensitive ultraviolet photodetector composed of double-layered *TiO*$_2$ nanostructure and Au nanoparticles film based on Schottky junction. *Mater. Chem. Phys.* **2017**, *194*, 42−48.

(19) Kavan, L. Conduction band engineering in semiconducting oxides (TiO2, SnO2): Applications in perovskite photovoltaics and beyond. *Catal. Today* **2019**, *328*, 50−56.

(20) Awazu, K.; Fujimaki, M.; Rockstuhl, C.; Tominaga, J.; Murakami, H.; Ohki, Y.; Yoshida, N.; Watanabe, T. A plasmonic photocatalyst

consisting of silver nanoparticles embedded in titanium dioxide. *J. Am. Chem. Soc.* **2008**, *130*, 1676−1680.
(21) Gao, F.; Yang, Y.; Wang, T. Preparation of porous TiO_2/Ag heterostructure films with enhanced photocatalytic activity. *Chem. Eng. J.* **2015**, *270*, 418−427.
(22) Khosravani, S.; Dehaghi, S. B.; Askari, M. B.; Khodadadi, M. The effect of various oxidation temperatures on structure of Ag-TiO_2 thin film. *Microelectron. Eng.* **2016**, *163*, 67−77.
(23) Liu, Z.; Siegel, J.; Garcia-Lechuga, M.; Epicier, T.; Lefkir, Y.; Reynaud, S.; Bugnet, M.; Vocanson, F.; Solis, J.; Vitrant, G.; et al. Three-dimensional self-organization in nanocomposite layered systems by ultrafast laser pulses. *ACS Nano* **2017**, *11*, 5031−5040.
(24) Wang, Q.; Xu, Y.; Zhang, S.; Gao, S.; Zheng, Q.; Yuan, Q.; Rong, W.; Yin, C.; Wang, J.; Wang, M. Self-organized TiO_2 nanotube arrays sensitized by uniform *Cd*0. 8*Zn*0.2*S* nanoparticles for highly effective photoelectrochemical performance. *Mater. Des.* **2016**, *92*, 102−106.
(25) Loeschner, K.; Seifert, G.; Heilmann, A. Self-organized, gratinglike nanostructures in polymer films with embedded metal nanoparticles induced by femtosecond laser irradiation. *J. Appl. Phys.* **2010**, *108*, 073114.
(26) Wu, D.; Xu, J.; Niu, L.-G.; Wu, S.-Z.; Midorikawa, K.; Sugioka, K. In-channel integration of designable microoptical devices using flat scaffold-supported femtosecond-laser microfabrication for coupling-free optofluidic cell counting. *Light: Sci. Appl.* **2015**, *4*, e228.
(27) Sharma, N.; Ma, H.; Bottein, T.; Bugnet, M.; Vocanson, F.; Grosso, D.; Itina, T. E.; Ouerdane, Y.; Destouches, N. Crystal growth in mesoporous TiO_2 optical thin films. *J. Phys. Chem. C* **2019**, *123*, 6070−6079.
(28) Rudenko, A.; Colombier, J.-P.; Itina, T. Femtosecond laser irradiation of fused silica with a nanometric inhomogeneity. *PIERS Proc.* **2015**, 1652−1656.
(29) Pyatenko, A.; Wang, H.; Koshizaki, N.; Tsuji, T. Mechanism of pulse laser interaction with colloidal nanoparticles. *Laser & Photonics Reviews* **2013**, *7*, 596−604.
(30) Kabashin, A. V.; Meunier, M. Synthesis of colloidal nanoparticles during femtosecond laser ablation of gold in water. *J. Appl. Phys.* **2003**, *94*, 7941−7943.
(31) Sylvestre, J.-P.; Kabashin, A. V.; Sacher, E.; Meunier, M. Femtosecond laser ablation of gold in water: influence of the laser-produced plasma on the nanoparticle size distribution. *Appl. Phys. A: Mater. Sci. Process.* **2005**, *80*, 753−758.
(32) Metwally, K.; Mensah, S.; Baffou, G. Fluence threshold for photothermal bubble generation using plasmonic nanoparticles. *J. Phys. Chem. C* **2015**, *119*, 28586−28596.
(33) Pustovalov, V. K. Theoretical study of heating of spherical nanoparticle in media by short laser pulses. *Chem. Phys.* **2005**, *308*, 103−108.
(34) Grady, D. The spall strength of condensed matter. *J. Mech. Phys. Solids* **1988**, *36*, 353−384.
(35) Rudenko, A.; Colombier, J.-P.; Itina, T. E. Nanopore-mediated ultrashort laser-induced formation and erasure of volume nanogratings in glass. *Phys. Chem. Chem. Phys.* **2018**, *20*, 5887−5899.
(36) Tang, H.-q.; Lin, Y.; Cheng, Z.-w.; Cui, X.-f.; Wang, B. Direct view of Cr atoms doped in anatase TiO_2 (001) thin film. *Chin. J. Chem. Phys.* **2018**, *31*, 71−76.
(37) Cheng, Z.; Zhang, L.; Dong, S.; Ma, X.; Ju, H.; Zhu, J.; Cui, X.; Zhao, J.; Wang, B. Electronic properties of Cr-N codoped rutile TiO_2 (110) thin films. *Surf. Sci.* **2017**, *666*, 84−89.
(38) Nadar, L.; Sayah, R.; Vocanson, F.; Crespo-Monteiro, N.; Boukenter, A.; Sao Joao, S.; Destouches, N. Influence of reduction processes on the colour and photochromism of amorphous mesoporous TiO_2 thin films loaded with a silver salt. *Photochemical & Photobiological Sciences* **2011**, *10*, 1810−1816.
(39) Mie, G. Beiträge zur optik trüber medien, speziell kolloidaler metallösungen. *Ann. Phys.* **1908**, *330*, 377−445.
(40) Bohren, C. F.; Huffman, D. R. *Absorption and scattering of light by small particles*; John Wiley & Sons: New York, 2008.
(41) Durović, M. D.; Puchta, R.; Bugarčić, Ž. D.; van Eldik, R. Studies on the reactions of [*AuCl* 4]- with different nucleophiles in aqueous solution. *Dalton Transactions* **2014**, *43*, 8620−8632.
(42) Plech, A.; Kotaidis, V.; Lorenc, M.; Boneberg, J. Femtosecond laser near-field ablation from gold nanoparticles. *Nat. Phys.* **2006**, *2*, 44.
(43) Manjavacas, A.; Liu, J. G.; Kulkarni, V.; Nordlander, P. Plasmon-induced hot carriers in metallic nanoparticles. *ACS Nano* **2014**, *8*, 7630−7638.
(44) Rudenko, A.; Colombier, J.-P.; Itina, T. E. Femtosecond laser irradiation of dielectric materials containing randomly-arranged nanoparticles. *Synthesis and Photonics of Nanoscale Materials XIII*; SPIE LASE, San Francisco, CA, 2016; p 97370L.
(45) Uskov, A. V.; Protsenko, I. E.; Ikhsanov, R. S.; Babicheva, V. E.; Zhukovsky, S. V.; Lavrinenko, A. V.; O'Reilly, E. P.; Xu, H. Internal photoemission from plasmonic nanoparticles: comparison between surface and volume photoelectric effects. *Nanoscale* **2014**, *6*, 4716−4727.
(46) Babicheva, V. E.; Zhukovsky, S. V.; Ikhsanov, R. S.; Protsenko, I. E.; Smetanin, I. V.; Uskov, A. Hot electron photoemission from plasmonic nanostructures: The role of surface photoemission and transition absorption. *ACS Photonics* **2015**, *2*, 1039−1048.
(47) Tagliabue, G.; Jermyn, A. S.; Sundararaman, R.; Welch, A. J.; DuChene, J. S.; Pala, R.; Davoyan, A. R.; Narang, P.; Atwater, H. A. Quantifying the role of surface plasmon excitation and hot carrier transport in plasmonic devices. *Nat. Commun.* **2018**, *9*, 3394.
(48) Graf, M.; Jalas, D.; Weissmüller, J.; Petrov, A. Y.; Eich, M. Surface-to-volume ratio drives photoelelectron injection from nano-scale gold into electrolyte. *ACS Catal.* **2019**, *9*, 3366−3374.
(49) Juvé, V.; Scardamaglia, M.; Maioli, P.; Crut, A.; Merabia, S.; Joly, L.; Del Fatti, N.; Vallée, F. Cooling dynamics and thermal interface resistance of glass-embedded metal nanoparticles. *Phys. Rev. B: Condens. Matter Mater. Phys.* **2009**, *80*, 195406.
(50) Werner, D.; Hashimoto, S. Improved working model for interpreting the excitation wavelength-and fluence-dependent response in pulsed laser-induced size reduction of aqueous gold nanoparticles. *J. Phys. Chem. C* **2011**, *115*, 5063−5072.
(51) Delfour, L.; Itina, T. E. Mechanisms of ultrashort laser-induced fragmentation of metal nanoparticles in liquids: numerical insights. *J. Phys. Chem. C* **2015**, *119*, 13893−13900.
(52) Dagallier, A.; Boulais, E.; Boutopoulos, C.; Lachaine, R.; Meunier, M. Multiscale modeling of plasmonic enhanced energy transfer and cavitation around laser-excited nanoparticles. *Nanoscale* **2017**, *9*, 3023−3032.
(53) Rudenko, A.; Colombier, J.-P.; Itina, T. E. Graphics processing unit-based solution of nonlinear Maxwell's equations for inhomogeneous dispersive media. *International Journal of Numerical Modelling: Electronic Networks, Devices and Fields* **2018**, *31*, e2215.
(54) Frese, K. W.; Chen, C. Theoretical models of hot carrier effects at metal-semiconductor electrodes. *J. Electrochem. Soc.* **1992**, *139*, 3234−3243.
(55) Brack, M. Multipole vibrations of small alkali-metal spheres in a semiclassical description. *Phys. Rev. B: Condens. Matter Mater. Phys.* **1989**, *39*, 3533.
(56) Ciraci, C.; Della Sala, F. Quantum hydrodynamic theory for plasmonics: impact of the electron density tail. *Phys. Rev. B: Condens. Matter Mater. Phys.* **2016**, *93*, 205405.
(57) Lin, Z.; Zhigilei, L. V.; Celli, V. Electron-phonon coupling and electron heat capacity of metals under conditions of strong electron-phonon nonequilibrium. *Phys. Rev. B: Condens. Matter Mater. Phys.* **2008**, *77*, 075133.
(58) Hüttner, B. *The Theory of Laser Materials Processing*; Springer: New York, 2009; pp 315−337.
(59) Chowdhury, I. H.; Xu, X. Heat transfer in femtosecond laser processing of metal. *Numer. Heat Transfer, Part A* **2003**, *44*, 219−232.
(60) Arbouet, A.; Voisin, C.; Christofilos, D.; Langot, P.; Del Fatti, N.; Vallée, F.; Lermé, J.; Celep, G.; Cottancin, E.; Gaudry, M.; et al. Electron-phonon scattering in metal clusters. *Phys. Rev. Lett.* **2003**, *90*, 177401.

https://dx.doi.org/10.1021/acs.jpcc.0c01092
J. Phys. Chem. C 2020, 124, 10209−10219

(61) Mongin, D.; Maioli, P.; Burgin, J.; Langot, P.; Cottancin, E.; D'addato, S.; Canut, B.; Treguer, M.; Crut, A.; Vallée, F.; et al. Ultrafast electron-lattice thermalization in copper and other noble metal nanoparticles. *J. Phys.: Condens. Matter* **2019**, *31*, 084001.
(62) Stoll, T.; Maioli, P.; Crut, A.; Del Fatti, N.; Vallée, F. Advances in femto-nano-optics: ultrafast nonlinearity of metal nanoparticles. *Eur. Phys. J. B* **2014**, *87*, 260.
(63) Simanovskii, D. M.; Schwettman, H. A.; Lee, H.; Welch, A. J. Midinfrared optical breakdown in transparent dielectrics. *Phys. Rev. Lett.* **2003**, *91*, 107601.
(64) Tang, M.; Hooper, J. P. Impact fragmentation of a brittle metal compact. *J. Appl. Phys.* **2018**, *123*, 175901.
(65) Yang, X.; Zhang, B. Material embrittlement in high strain-rate loading. *International Journal of Extreme Manufacturing* **2019**, *1*, 022003.

https://dx.doi.org/10.1021/acs.jpcc.0c01092
J. Phys. Chem. C 2020, 124, 10209−10219